

Three-dimensional time-reversal invariant topological superconductivity in doped chiral topological semimetals

Yingyi Huang¹ and Shao-Kai Jian^{1,2}

¹*Institute for Advanced Study, Tsinghua University, Beijing 100084, China*

²*Condensed Matter Theory Center Maryland, Department of Physics, University of Maryland, College Park, MD 20742, USA*

(Dated: June 14, 2022)

Chiral topological semimetals host multifold degenerate band crossing points under the protection of crystalline symmetries. In this paper, we suggest the recently discovered chiral topological semimetals in space group $P2_13$ (No. 198), parts of which are superconducting upon doping, can be new candidates of time-reversal-invariant topological superconductors. By investigating the Fermi surfaces around the band crossing points, we clarify how the nontrivial topology of chiral topological semimetals affects their superconducting state and show the existence of topological superconductivity with surface Majorana fermions. We further demonstrate that the topological superconductivity is favored by inter-unit cell phonon-mediated electron-electron interaction.

Over the last decade, the interplay of superconductor pairing and band topology has paved a route to topological superconductors (TSC) hosting Majorana modes, which have potential applications in topological quantum computation [1–12]. This intriguing interplay can be realized as a result of the proximity of conventional s -wave superconductor (SC) and one dimensional (1D) spin-orbit coupled semiconductor [13–15] or 2D topological insulator [16]. Despite the fact that experimental progress have been made [17–19], the heterostructures make confirmation and further application complicated. On the other hand, superconductivity is allowed to exist in topological (crystalline) insulator under doping, pressure, or low temperature. The famous examples include CuBi_2Se_3 [20–22] and $\text{Sn}_{1-x}\text{In}_x\text{Te}$ [23]. This mechanism also applies to gapless topological matters (e.g., doped Weyl and Dirac semimetals) [24, 25]. Although zero-bias conductance peaks have been experimentally observed [28–32] in iron-based superconductors in gapless system, further investigation on superconducting topological matter is necessary.

Recently, another type of gapless topological matters in crystals with specific non-symmorphic space group symmetry, dubbed as “chiral topological semimetals” or chiral crystals [33–35], have attracted a lot of experimental attentions [36–40]. The chiral topological semimetals can be viewed as natural generalization of the well-studied Weyl semimetal. In particular, in low-energy Hamiltonian of Weyl semimetal $H = \delta \mathbf{k} \cdot \mathbf{S}$, the spin-1/2 vector \mathbf{S} is replaced by spin-1 or -3/2 matrices in chiral topological semimetals [33–35]. However, the chiral topological semimetals have distinguished bulk and edge topological properties. Different from the chiral fermion in spin-1/2 Weyl fermion with a topological charge (Chern number) $C = \pm 1$, the chiral fermions in chiral topological semimetals are multifold and carry topological charge C larger than 1. For instance, the chiral topological semimetals in space group $P2_13$ host 4- and 6-fold chiral fermions as shown in Fig. 1(a) and (b). While

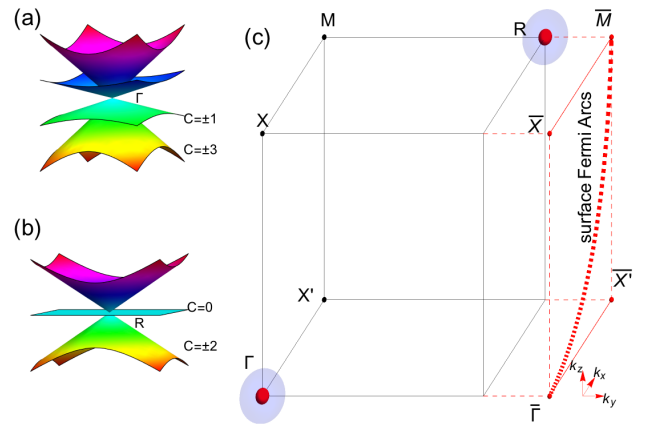


FIG. 1. (Color online) Energy dispersion for the chiral topological semimetal in space group $P2_13$ of (a) four-fold degeneracy at the Γ point and (b) six-fold degeneracy at the R point. (c) The Brillouin zone with Fermi surfaces around Γ and R point paired by s_{\pm} -wave pairing SC. The projected BZ of the (001) surface is marked in red lines with the projected Fermi arcs in dashed line.

the band crossings of Weyl semimetal are positioned at Weyl points away from the high-symmetry points of the Brillouin zone, the high-order degenerated band crossing point of chiral topological semimetal are located at high-symmetry points. In space group $P2_13$, the multifold nodes at Γ and R are connected by a long Fermi arcs [see Fig. 1(c)].

In analog with TSC in doped Weyl semimetal, it is natural to expect interesting superconducting states to emerge in these topological chiral semimetal systems upon doping. In this paper we address the effect of the nontrivial topology, i.e., the high symmetric points and Fermi arcs, on the superconducting properties. The fact that the source (positive Chern number) and sink (negative Chern number) of Berry curvature are located at high symmetric points (e.g., in space group $P2_13$,

$C = \pm 4$ at Γ and R points), establishing that the doped chiral topological semimetals favor an unconventional SC pairing rather than a conventional s -wave one. Also the high Chern number in normal state gives a large topological number in SC state of chiral topological semimetals, which is distinguished from that of Weyl semimetals. In the superconducting state, surface Majorana fermion stemming the surface Fermi arcs in the normal state. In contrast to the Weyl semimetal, the open Fermi arcs of chiral topological semimetal intersect with the diagonal axis of surface BZ instead of edge axis. As a result, the position of surface Majorana fermion in momentum space is different.

Recently, isotropic s -wave and isotropic d -wave superconducting state of the fourfold linear band-crossing point in the chiral topological semimetal are theoretical investigated [41, 42]. However, the analysis is focus on unconventional superconductivity and neglect the topology around R point. To investigate the possible topological superconductivity, the non-symmorphic space group symmetry should be taken into account instead of little point-group symmetry around Γ point. In this work, we propose that doped chiral topological semimetals are natural hosts for realizing a time-reversal invariant TSC. We specify the Fermi surfaces of chiral topological semimetal and reveal that the realization of topological superconductivity requires a momentum-dependent superconducting pairing, rather than a conventional s -wave one. By carefully examining a Hamiltonian preserving space group symmetry, we find that a s_{\pm} -wave superconducting pairing is topological non-trivial and fully gapped.

Fermi surfaces around the nodes.— We begin with an analysis of the topology of band-crossing points. The materials in SG $P2_13$ are protected by a diagonal cubic threefold rotation $C_{3,111}$ and two two-fold screw rotation symmetries C_{2x} and C_{2z} . The non-symmorphic space group symmetries lead to multiply band crossing at two time-reversal-invariant points: the BZ center Γ point and the BZ corner R point. The existence of these two multifold Weyl nodes are also ensured by the nonzero Chern number of bands below the Fermi level around these points. At chemical potential below the Fermi level, the topological charge of the occupied bands is +3 and +1 at Γ point and -2 and -2 at R point. The total topological charge at Γ and R is ± 4 respectively. The fact that their sum is zero is consistent with the Nielsen-Ninomiya no-go theorem [43].

With a finite carrier density, disconnected Fermi surfaces appear surround Γ and R points in the chiral topological semimetal. We consider a case with four Fermi surfaces above chemical potential: at Γ point the Fermi surfaces with Chern number $\mathcal{C} = 3$ and $\mathcal{C} = 1$; at R point, the Fermi surface with $\mathcal{C} = -2$ who is its own time-reversal partner. According to topological classification [44], a three-dimensional(3D) time-reversal invari-

ant superconductor in class DIII is characterized by an integer (\mathbb{Z}) topological invariant, which can be written as a winding number over the entire momentum space. To characterize the topological properties of bulk wave function, the winding number for a 3D topological superconductor is defined as [45]:

$$\nu = \frac{1}{24\pi^2} \int d^3\mathbf{k} \epsilon^{ijk} \text{Tr} \left[Q_{\mathbf{k}}^\dagger \partial_i Q_{\mathbf{k}} Q_{\mathbf{k}}^\dagger \partial_j Q_{\mathbf{k}} Q_{\mathbf{k}}^\dagger \partial_k Q_{\mathbf{k}} \right]. \quad (1)$$

Here, $Q_{\mathbf{k}}$ is related to the projection operator of occupied state $P_{\mathbf{k}} = \sum_{n \in \text{filled}} |u_{n\mathbf{k}}\rangle \langle u_{n\mathbf{k}}|$ as $Q_{\mathbf{k}} = 1 - P_{\mathbf{k}}$ with $|u_{n\mathbf{k}}\rangle$ being the n -th Bloch wave function at \mathbf{k} .

To relate the winding number to the Chern numbers on Fermi surfaces, we consider a simple case: When the superconducting gap is much smaller than the Fermi energy, the topological properties of the possible superconductor pairing completely determined by the the properties in the neighborhood of the Fermi surface [46]. Under this weak pairing assumption, the winding number for a topological superconductor is defined as

$$\nu = \frac{1}{2} \sum_{j \in \text{FS}} C_j \text{sgn}(\Delta_j). \quad (2)$$

Under the time-reversal symmetry, the SC pairing gap function Δ_j on the j -th surface is real and is well-defined for a gapped system.

The huge separation of Γ and R critically affects the possible superconductor pairing between electrons. Indeed, we can show that s -wave pairing local in space is topological trivial. The s -wave SC pairing gap functions on all the Fermi surfaces are all positive or all negative. Since the total Chern number for all the Fermi surfaces in the BZ is zero guaranteed by the no-go theorem [43], the winding number is zero for all the momentum-independent SC pairing potential. To obtain a nonzero winding number, a momentum-dependent pairing potential is required. In particular, the s_{\pm} -wave Cooper pair is compatible with the Fermi surfaces topology of chiral topological semimetal. The s_{\pm} -wave pairing between electrons on different orbitals of the Fermi surfaces is around Γ and R points and the sign of pairing amplitude changes between Γ and R points and thus provides a non-zero winding number. The s_{\pm} -wave SC pairing is a spin-singlet state and can be written in a form as

$$\Delta(\mathbf{k}) = id(\mathbf{k})\sigma_y \quad (3)$$

In noncentrosymmetric superconductors whose inversion symmetry is broken, parity is ill-defined. Here, $d(\mathbf{k})$ is an even functions of \mathbf{k} and forms a irreducible representation of space group. For simplify, it can be chosen to be $d(\mathbf{k}) = \Delta_0 (\cos(k_x) + \cos(k_y) + \cos(k_z))$ corresponding to A representation of space group $P2_13$. As anticipated, the s_{\pm} -wave SC pairing gives a TSC with $\nu = 4$.

Note that since the inversion symmetry is broken in the system, one cannot apply the criterion for odd-parity superconductor [20]. And for a 3D time-reversal-invariant TSC in class DIII, the \mathbb{Z} classification of band theory reduces to a \mathbb{Z}_{16} classification with interactions [47].

Low-energy analysis. – For definiteness, we study a low-energy effective Hamiltonian respects time-reversal symmetry \mathcal{T} and non-symmorphic symmetries. The generators are described by a point group \mathbb{T} in combination with the translational parts. In the presence of the translational parts, the generators at different high-symmetric points are distinguished. In particular, the generators at Γ point are $s_{2x} = \{C_{2x}|\frac{1}{2}\frac{1}{2}0\}$, $s_{2z} = \{C_{2z}|\frac{1}{2}0\frac{1}{2}\}$, $s_{3,111} = \{C_{3,111}|000\}$ with \mathcal{K} the complex conjugation. At R point, the generators become $s_{2x} = \{C_{2x}|\frac{1}{2}\frac{3}{2}0\}$, $s_{2z} = \{C_{2z}|\frac{3}{2}0\frac{1}{2}\}$, $s_{3,111} = \{C_{3,111}|010\}$. Thus, to capture the topological properties of the Fermi surfaces around Γ and R point, the Hamiltonian should be allowed by the space group symmetries instead of a little point group symmetries near one of the band touching points.

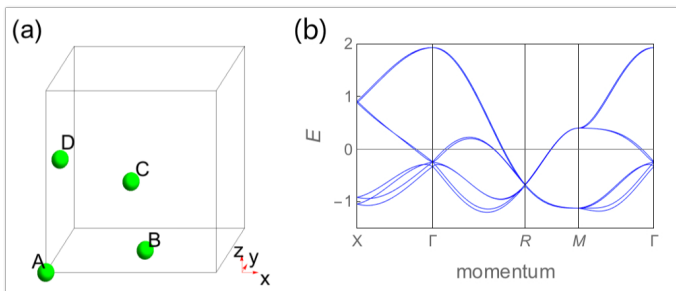


FIG. 2. (Color online) (a) The lattice structure in real space. The orbitals $A(0,0,0)$, $B(\frac{1}{2}, \frac{1}{2}, 0)$, $C(\frac{1}{2}, 0, \frac{1}{2})$ and $D(0, \frac{1}{2}, \frac{1}{2})$ in the same unit cell are marked in green, while the orbital in the adjacent unit cells are in purple. (b) Reproduction the band dispersion of RhSi [34] along a typical high symmetric cut in the BZ.

The insulating filling constraint for spin-orbit coupled insulators in space group $P2_13$ is $\nu \in 8\mathbb{Z}$ according to Ref. [48]. It indicates the tight-binding model should be described by a 8×8 matrix Hamiltonian. The Hamiltonian can be written in a basis of spin σ and four Wannier orbitals in a unit-cell shown in Fig. 2(a). The Pauli matrix τ^x represents hopping between orbitals A and B , or between orbitals C and D . Similarly, μ^x represents hopping between A and C , or B and D . Under the basis (c^A, c^C, c^B, c^D) , the operations can be written as $s_{2x} = i\tau^x \sigma^x \otimes (k_{y,z} \rightarrow -k_{y,z})$, $s_{2z} = i\mu^x \sigma^z \otimes (k_{x,y} \rightarrow -k_{x,y})$, $\mathcal{T} = i\sigma^y \mathcal{K} \otimes (k_{x,y,z} \rightarrow -k_{x,y,z})$ and $C_{3,111} = \begin{pmatrix} 1 & 0 & 0 & 0 \\ 0 & 0 & 1 & 0 \\ 0 & 0 & 0 & 1 \\ 0 & 1 & 0 & 0 \end{pmatrix} e^{i\sigma_{111}/3} \otimes (k_x \rightarrow k_y, k_y \rightarrow k_z, k_z \rightarrow k_x)$ with $\sigma_{111} = (\sigma_x + \sigma_y + \sigma_z)/\sqrt{3}$. The full expression for the lattice model H_0 is given in the Supplemental Mate-

rial (SM).

In Fig. 2(b), we reproduce the band dispersion of RhSi. We can see that there is a six-fold degeneracy at Γ and a four-fold degeneracy at R , in consistency with the ARPES measurement [36–38]. In addition, the calculation of Eq. 1 results topological invariant $\nu = 4$, in agreement with the analytical analysis. Note that the results only depend on the Fermi surface topology, but not on the fine-tuning of parameters.

To show the existence of topological protected gapless edge states, we write down the BdG Hamiltonian

$$H_{\text{BdG}}(\mathbf{k}) = \begin{pmatrix} H_0(\mathbf{k}) - \mu & \Delta(\mathbf{k}) \\ \Delta^\dagger(\mathbf{k}) & -H_0^\dagger(\mathbf{k}) + \mu \end{pmatrix}. \quad (4)$$

Here, μ is the chemical potential corresponding to the finite carrier density. This BdG Hamiltonian supports particle-hole symmetry, $CH_{\text{BdG}}(\mathbf{k})C^{-1} = -H_{\text{BdG}}(-\mathbf{k})$, and the time-reversal symmetry, $TH_{\text{BdG}}(\mathbf{k})T^{-1} = H_{\text{BdG}}(-\mathbf{k})$. The particle-hole symmetry operator and time-reversal symmetry operator are given by $C = \rho_x \mathcal{K}$ and $T = \rho_0 \mathcal{T}$ of which ρ_α is the Pauli matrices representing particle-hole degree of freedom. The BdG Hamiltonian retains all the symmetries of the chiral topological semimetals, including the non-symmorphic symmetries.

In the presence of the s_{\pm} -wave SC, we found that the chiral topological semimetal become a fully bulk-gapped TSC by numerically calculate the energy spectrum the BdG Hamiltonian with Eq. 4. Due to the bulk-edge correspondence, we expect the existence of gapless modes at a 2D surface as a manifest of the nontrivial topological properties of a 3D TSC. To show this, we consider a geometry with periodic boundary conditions in the x and z directions and the open one in the y direction. From the surface energy spectrum is shown in Fig. 3(a), one can see that there are gapless states. They are located at the surface Fermi arcs connecting $\bar{\Gamma}$ and \bar{M} . Note that the momentum space position of Majorana fermions in TSC on doped chiral topological semimetals is different from that in TSC on doped chiral Weyl semimetals

Figure 3(b) shows that there are four pairs of helical Majorana states crossing the bulk superconducting gap along the $\bar{X} - \bar{X}'$ cut on the $(0\ 1\ 0)$ plane. The right-going and left-going states are spin splitting and localized at opposite edges. Note that the four states at one edge in the (001) plane are protected by the skew rotation symmetry and only two double-degenerate states could be seen.

Interaction. – As we have shown that a doped chiral topological semimetal with a s_{\pm} -wave pairing state can be a natural host for realization a topological superconductor, it is necessary to examine the stability of the pairing state. We will investigate the microscopic interaction that favors this s_{\pm} -wave state using the fluctuation-exchange approach [24] and considering onsite interaction and momentum-dependent interaction up to first order. Three kinds of interactions will be included: the

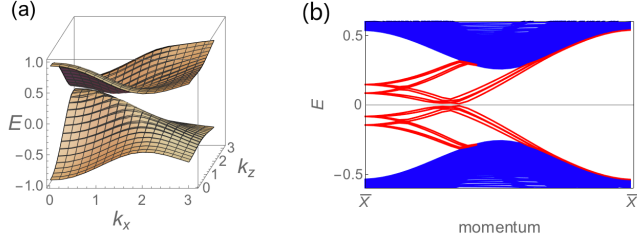


FIG. 3. (Color online) The low-energy BdG spectra for (0 1 0) surface with SC pairing amplitude $\Delta = 0.2$. The red solid lines indicates the helical electron edge modes. The parameters are the same with Fig. 2.

effective intra-orbital onsite interaction U , the effective inter-orbital interaction V , and effective intra-orbital interaction between adjacent unit cells W . The effective interaction parameters are given by the difference between electron-phonon coupling I_{ph} and Coulomb repulsion I_{coul} as $I = I_{\text{ph}} - I_{\text{coul}}$, $I = U, V, W$. The interactions as follows,

$$H_{\text{int}} = -U \sum_{i,l} n_{il} n_{il} - V \sum_{i,l \neq l'} n_{il} n_{il'} - W \sum_{\langle i,i' \rangle, l, \sigma \neq \sigma'} C_{il\sigma}^\dagger C_{il'\sigma'}^\dagger C_{i'l\sigma} C_{i'l'\sigma'},$$

where l indices are summed over all the s -wave orbitals in one unit cell ($l = A, B, C, D$). $n_{il} = \sum_{\sigma} C_{il\sigma}^\dagger C_{il\sigma}$ is the electron density with spin $\sigma = \uparrow, \downarrow$ locating at sublattice l in the unit cell i .

In the BCS theory, if we start from a free electron gas, and turn on an attractive interaction. The system becomes unstable and the electrons will group themselves in pairs giving up energy to the external world. Two electrons in plane wave states $\psi_{\mathbf{k}}$ and $\psi_{-\mathbf{k}}$ scatter toward final states $\psi_{\mathbf{k}'}$ and $\psi_{-\mathbf{k}'}$. Thus, the inter-unit cell interaction W is necessary to guarantee the s_{\pm} pairing between electrons in Γ and R points at different momentum $\mathbf{k} = (0, 0, 0)$ and $\mathbf{k}' = (\pi, \pi, \pi)$.

Since the chiral topological semimetal preserves the time-reversal symmetry, the pairing of Cooper pair $\psi_{\mathbf{k}}$ and $\psi_{-\mathbf{k}}$ can only occur between the Fermi surfaces which are a pair of Kramer's partner. Indeed, the interaction projected onto the Fermi surfaces takes the following form:

$$\chi^{ij}(\mathbf{k}, \mathbf{k}') = \langle \psi_{\mathbf{k}',j} | \otimes \langle \mathcal{T} \psi_{\mathbf{k}',j} | H_{\text{int}}(\mathbf{k}, \mathbf{k}') | \mathcal{T} \psi_{\mathbf{k},i} \rangle \otimes | \psi_{\mathbf{k},i} \rangle \quad (5)$$

where $|\psi_{\mathbf{k},i}\rangle$ being one of the following four wavefunctions for the Fermi level states $\{|\psi_{\Gamma,3/2}\rangle, |\psi_{\Gamma,1/2}\rangle, |\psi_{R,-2}\rangle, |\mathcal{T}\psi_{R,-2}\rangle^*\}$. The construction of these wavefunctions are presented in the Supplemental Material (SM).

From the effective interaction, we obtain the pairing

order parameter by solving the linearized gap equation

$$\sum_j \int_k' \delta(v_j \delta k') \chi^{ij}(k, k') \Delta_j(k') = \lambda \Delta_i(k) \quad (6)$$

where $\int_k' \equiv \int \frac{d^3 k'}{(2\pi)^3}$ sum over the fermi surface. The most negative eigenvalue λ gives the highest $T_c \propto \exp(-1/\lambda)$ and determines the dominant pairing. And its corresponding eigenvector gives the pairing order parameter Δ_j . In particular, the signs of the pairing order on different Fermi surfaces and the winding number are related by Eq. (2), which characterizes the SC pairing phase.

The phase diagrams as a function of onsite interactions $U(V)$ and neighbor unit-cell interaction W are shown in Fig. 4. First, the phase diagram for onsite intra-orbital interaction U is plotted in Fig. 4(a). The s_{\pm} -wave SC pairing is favored by negative U and positive W . This indicates that the topological nontrivial s_{\pm} -wave pairing exists only when the onsite Coulomb repulsion is stronger than electron-phonon coupling and the inter-unit-cell electron-phonon coupling is stronger than Coulomb interaction. In contrast, the conventional s -wave pairing which is inter-orbital spin-singlet, it is favored by the attractive onsite intra-orbital interaction. And the system is in a metal phase with $\Delta = 0$ when there is no correlations. Second, in Fig. 4(b), the inter unit-cell s_{\pm} phase wins as long as the inter-unit cell interaction is positive and exceeds the onsite inter-orbital interaction $W > |V|$. Therefore, when there is electron correlation between neighbor electron correlation and the onsite interaction is constrained, the s_{\pm} -wave SC pairing is preferred.

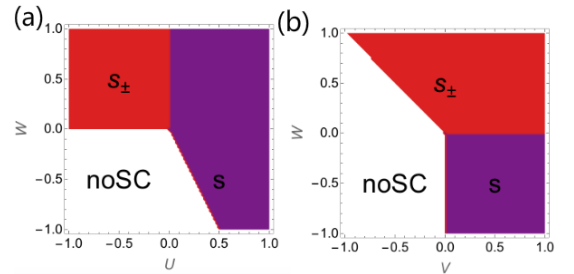


FIG. 4. (Color online) The phase diagram for inter-unit cell interaction W and onsite (a) intra-orbital interaction U and (b) inter-orbital interaction V respectively. Only the most leading channel at each point is indicated: s_{\pm} -wave pairing (red), s -wave pairing (purple).

Materials.— The chiral topological semimetals can be realized in materials with time-reversal symmetry and spin-orbit coupling and their host of crystal symmetry-protected fermionic excitations are stabilized by non-symmorphic symmetries [33]. The most considered chiral crystals are in space group $P2_13$ (No. 198) primitive cubic lattice [34, 35]. Recently, chiral topological

semimetals have been experimental found with the observation of long Fermi arcs by angle-resolved photoemission spectroscopy (ARPES) in several materials of space group $P2_13$, including CoSi [36–38], RhSi [38], PtGa [49], PdGa [50], AIPt [39], and PdBiSe [40].

Superconducting phase transitions were reported in AuBe and PdBiSe, two compounds in the cubic $P2_13$ space group. AuBe, a transition metal compound, has been predicted to host unconventional fermions due to its calculated electronic structure [51]. It exhibits superconductivity under low temperature (3.3K) with time-reversal symmetry being preserved [52]. On the other hand, ARPES measurement has observed multiple unconventional fermions in PdBiS, an Ullmannite-type compound [40]. And bulk PdBiSe has been claimed to undergo a superconducting transition below 1.8 K [53].

Conclusion. – We have revealed that 3D time-reversal invariant TSC phase can be realized in a doped chiral topological semimetal. In particular, we have shown the existence of TSC phase with $\nu = 4$ in chiral topological semimetals of space group $P2_13$ by calculating topological invariant and BdG spectrum. Our work on realizing TSC in topological chiral semimetal opens the door to advances in the study of spin triplet pairing and their application to quantum information technology. The possible Majorana excitations hosing in the chiral topological semimetal can be detected by angle-resolved photoemission spectroscopy or scanning tunneling microscope.

Acknowledgements. – We thank Zhong Wang for suggesting this project to us. Y. H. is indebted to Baiqing Lv, Lingyuan Kong, Zhongbo Yan, Ailei He, and Ching-Kai Chiu for helpful discussions.

-
- [1] C. Nayak, S. H. Simon, A. Stern, M. Freedman, and S. Das Sarma, *Rev. Mod. Phys.* **80**, 1083 (2008).
- [2] S. D. Sarma, M. Freedman, and C. Nayak, *Npj Quantum Information* **1**, 15001 EP (2015).
- [3] J. Alicea, *Reports on Progress in Physics* **75**, 076501 (2012).
- [4] S. R. Elliott and M. Franz, *Rev. Mod. Phys.* **87**, 137 (2015).
- [5] T. D. Stanescu and S. Tewari, *J. Phys.: Condens. Matter* **25**, 233201 (2013).
- [6] M. Leijnse and K. Flensberg, *Semicond. Sci. Technol.* **27**, 124003 (2012).
- [7] C. Beenakker, *Annu. Rev. Condens. Matter Phys.* **4**, 113 (2013).
- [8] R. Lutchyn, E. Bakkers, L. Kouwenhoven, P. Krogstrup, C. Marcus, and Y. Oreg, arXiv:1707.04899 (2017).
- [9] J.-H. Jiang and S. Wu, *Journal of Physics: Condensed Matter* **25**, 055701 (2013).
- [10] M. Sato and S. Fujimoto, *J. Phys. Soc. Jpn.* **85**, 072001 (2016).
- [11] M. Sato and Y. Ando, arXiv:1608.03395 (2016).
- [12] R. Aguado, arXiv:1711.00011 (2017).
- [13] J. D. Sau, R. M. Lutchyn, S. Tewari, and S. Das Sarma, *Phys. Rev. Lett.* **104**, 040502 (2010).
- [14] R. M. Lutchyn, J. D. Sau, and S. Das Sarma, *Phys. Rev. Lett.* **105**, 077001 (2010).
- [15] Y. Oreg, G. Refael, and F. von Oppen, *Phys. Rev. Lett.* **105**, 177002 (2010).
- [16] L. Fu and C. L. Kane, *Phys. Rev. Lett.* **100**, 096407 (2008).
- [17] V. Mourik, K. Zuo, S. M. Frolov, S. Plissard, E. P. A. M. Bakkers, and L. P. Kouwenhoven, *Science* **336**, 1003 (2012).
- [18] H. Zhang, C.-X. Liu, S. Gazibegovic, D. Xu, J. A. Logan, G. Wang, N. Van Loo, J. D. Bommer, M. W. De Moor, D. Car, *et al.*, *Nature* **556**, 74 (2018).
- [19] F. Nichele, A. C. C. Drachmann, A. M. Whiticar, E. C. T. O’Farrell, H. J. Suominen, A. Fornieri, T. Wang, G. C. Gardner, C. Thomas, A. T. Hatke, P. Krogstrup, M. J. Manfra, K. Flensberg, and C. M. Marcus, *Phys. Rev. Lett.* **119**, 136803 (2017).
- [20] L. Fu and E. Berg, *Phys. Rev. Lett.* **105**, 097001 (2010).
- [21] S. Sasaki, M. Kriener, K. Segawa, K. Yada, Y. Tanaka, M. Sato, and Y. Ando, *Phys. Rev. Lett.* **107**, 217001 (2011).
- [22] N. Levy, T. Zhang, J. Ha, F. Sharifi, A. A. Talin, Y. Kuk, and J. A. Stroscio, *Phys. Rev. Lett.* **110**, 117001 (2013).
- [23] M. Novak, S. Sasaki, M. Kriener, K. Segawa, and Y. Ando, *Physical Review B* **88**, 140502 (2013).
- [24] P. Hosur, X. Dai, Z. Fang, and X.-L. Qi, *Physical Review B* **90**, 045130 (2014).
- [25] S. Kobayashi and M. Sato, *Phys. Rev. Lett.* **115**, 187001 (2015).
- [26] Z. Wang, P. Zhang, G. Xu, L. K. Zeng, H. Miao, X. Xu, T. Qian, H. Weng, P. Richard, A. V. Fedorov, H. Ding, X. Dai, and Z. Fang, *Phys. Rev. B* **92**, 115119 (2015).
- [27] G. Xu, B. Lian, P. Tang, X.-L. Qi, and S.-C. Zhang, *Phys. Rev. Lett.* **117**, 047001 (2016).
- [28] D. Wang, L. Kong, P. Fan, H. Chen, S. Zhu, W. Liu, L. Cao, Y. Sun, S. Du, J. Schneeloch, R. Zhong, G. Gu, L. Fu, H. Ding, and H.-J. Gao, *Science* **362**, 333 (2018).
- [29] P. Zhang, K. Yaji, T. Hashimoto, Y. Ota, T. Kondo, K. Okazaki, Z. Wang, J. Wen, G. D. Gu, H. Ding, and S. Shin, *Science* **360**, 182 (2018).
- [30] C. Chen, Q. Liu, T. Z. Zhang, D. Li, P. P. Shen, X. L. Dong, Z.-X. Zhao, T. Zhang, and D. L. Feng, *Chinese Physics Letters* **36**, 057403 (2019).
- [31] T. Machida, Y. Sun, S. Pyon, S. Takeda, Y. Kohsaka, T. Hanaguri, T. Sasagawa, and T. Tamegai, *Nature Materials* **18**, 811 (2019).
- [32] Q. Liu, C. Chen, T. Zhang, R. Peng, Y.-J. Yan, C.-H.-P. Wen, X. Lou, Y.-L. Huang, J.-P. Tian, X.-L. Dong, G.-W. Wang, W.-C. Bao, Q.-H. Wang, Z.-P. Yin, Z.-X. Zhao, and D.-L. Feng, *Phys. Rev. X* **8**, 041056 (2018).
- [33] B. Bradlyn, J. Cano, Z. Wang, M. Vergniory, C. Felser, R. J. Cava, and B. A. Bernevig, *Science* **353**, aaf5037 (2016).
- [34] G. Chang, S.-Y. Xu, B. J. Wieder, D. S. Sanchez, S.-M. Huang, I. Belopolski, T.-R. Chang, S. Zhang, A. Bansil, H. Lin, *et al.*, *Physical review letters* **119**, 206401 (2017).
- [35] P. Tang, Q. Zhou, and S.-C. Zhang, *Physical review letters* **119**, 206402 (2017).
- [36] Z. Rao, H. Li, T. Zhang, S. Tian, C. Li, B. Fu, C. Tang, L. Wang, Z. Li, W. Fan, *et al.*, *Nature* **567**, 496 (2019).
- [37] D. Takane, Z. Wang, S. Souma, K. Nakayama, T. Nakamura, H. Oinuma, Y. Nakata, H. Iwasawa, C. Cacho, T. Kim, *et al.*, *Physical review letters* **122**, 076402 (2019).

- [38] D. S. Sanchez, I. Belopolski, T. A. Cochran, X. Xu, J.-X. Yin, G. Chang, W. Xie, K. Manna, V. Süß, C.-Y. Huang, *et al.*, *Nature* **567**, 500 (2019).
- [39] N. B. Schröter, D. Pei, M. G. Vergniory, Y. Sun, K. Manna, F. de Juan, J. A. Krieger, V. Süß, M. Schmidt, P. Dudin, *et al.*, *Nature Physics*, 1 (2019).
- [40] B. Lv, Z.-L. Feng, J.-Z. Zhao, N. F. Yuan, A. Zong, K. Luo, R. Yu, Y.-B. Huang, V. Strocov, A. Chikina, *et al.*, *Physical Review B* **99**, 241104 (2019).
- [41] I. Boettcher, *Physical Review Letters* **124**, 127602 (2020).
- [42] J. M. Link, I. Boettcher, and I. F. Herbut, *Physical Review B* **101**, 184503 (2020).
- [43] H. Nielsen and M. Ninomiya, *Physics Letters B* **105**, 219 (1981).
- [44] C.-K. Chiu, J. C. Y. Teo, A. P. Schnyder, and S. Ryu, *Rev. Mod. Phys.* **88**, 035005 (2016).
- [45] A. P. Schnyder, S. Ryu, A. Furusaki, and A. W. Ludwig, *Physical Review B* **78**, 195125 (2008).
- [46] X.-L. Qi, T. L. Hughes, and S.-C. Zhang, *Phys. Rev. B* **81**, 134508 (2010).
- [47] C. Wang and T. Senthil, *Physical Review B* **89**, 195124 (2014).
- [48] H. Watanabe, H. C. Po, A. Vishwanath, and M. Zaletel, *Proceedings of the National Academy of Sciences* **112**, 14551 (2015).
- [49] M. Yao, K. Manna, Q. Yang, A. Fedorov, V. Voroshnin, B. V. Schwarze, J. Hornung, S. Chattopadhyay, Z. Sun, S. N. Guin, *et al.*, *Nature Communications* **11**, 1 (2020).
- [50] N. Schröter, S. Stolz, K. Manna, F. de Juan, M. G. Vergniory, J. A. Krieger, D. Pei, P. Dudin, T. K. Kim, C. Cacho, *et al.*, arXiv preprint arXiv:1907.08723 (2019).
- [51] D. J. Rebar, S. M. Birnbaum, J. Singleton, M. Khan, J. Ball, P. Adams, J. Y. Chan, D. Young, D. A. Browne, and J. F. DiTusa, *Physical Review B* **99**, 094517 (2019).
- [52] A. Amon, E. Svanidze, R. Cardoso Gil, M. N. Wilson, H. Rosner, M. Bobnar, W. Schnelle, J. W. Lynn, R. Gumeniuk, C. Hennig, *et al.*, *Physical Review B* **97**, 1 (2018).
- [53] B. Joshi, A. Thamizhavel, and S. Ramakrishnan, in *Journal of Physics Conference Series*, Journal of Physics Conference Series, Vol. 592 (2015) p. 012069, arXiv:1410.4459 [cond-mat.supr-con].

Supplemental Material

I. THE EFFECTIVE TIGHT-BINDING MODEL

To characterize the chiral topological semimetals protecting by non-symmorphic space group symmetries, it is necessary to construct a effective tight-binding model instead of $\mathbf{k} \cdot \mathbf{p}$ models around high-symmetry points. Although the $\mathbf{k} \cdot \mathbf{p}$ models manifest the degeneracies of the high-spin fermions hosting in a material, it does not determine all the key properties of the material. The band dispersion away from the high-symmetry point, and any band crossings in the dispersion are also fundamental properties of the material.

While the $\mathbf{k} \cdot \mathbf{p}$ Hamiltonian is constructed from the irreducible representations of the little group at high-symmetry invariant, the tight-binding model is based on the representations of the space group. The representations of space group is constructed from non-symmorphic symmetries operators, which are combining operators from a point group operation followed by a translation. In particular, the representations of space group $P2_13$ are build on representations of point group \mathbb{T} (No. 23) and translational operators. To start, we can write down \mathbb{T} representations of point group \mathbb{T} :

$$\begin{aligned} & \{ \sigma_x, \sigma_y, \sigma_z \} \\ & \{ \tau_x, \tau_x \mu_x, \mu_x \} \\ & \{ \tau_y, \tau_x \mu_y, \tau_z \mu_y \} \\ & \{ \tau_y \mu_z, \tau_y \mu_x, \mu_y \} \\ & \{ \tau_x \mu_z, -\tau_y \mu_y, \tau_z \mu_x \} \end{aligned}$$

Here, the Pauli matrices σ_α and τ_α ($\alpha = x, y, z$) are defined in the main text.

Based on the irreducible representation theory, we can obtain the terms preserving space group symmetry as product of \mathbb{T} representation of point group and momentum. With momentum up to second order, the tight-binding model

firstly represented in Ref. 34 is

$$\begin{aligned}
H_0 = & v_1[\tau^x \cos \frac{k_x}{2} \cos \frac{k_y}{2} + \tau^x \mu^x \cos \frac{k_y}{2} \cos \frac{k_z}{2} + \mu^x \cos \frac{k_z}{2} \cos \frac{k_x}{2}] \\
& + v_p[\tau^y \mu^z \cos \frac{k_x}{2} \sin \frac{k_y}{2} + \tau^y \mu^x \cos \frac{k_y}{2} \sin \frac{k_z}{2} + \mu^y \cos \frac{k_z}{2} \sin \frac{k_x}{2}] \\
& + v_{r1}[\tau^y \mu^z \sigma^y \cos \frac{k_x}{2} \cos \frac{k_y}{2} + \tau^y \mu^x \sigma^z \cos \frac{k_y}{2} \cos \frac{k_z}{2} + \mu^y \sigma^x \cos \frac{k_z}{2} \cos \frac{k_x}{2}] \\
& + v_{r2}[\tau^y \sigma^z \cos \frac{k_x}{2} \cos \frac{k_y}{2} + \tau^x \mu^y \sigma^x \cos \frac{k_y}{2} \cos \frac{k_z}{2} + \tau^z \mu^y \sigma^y \cos \frac{k_z}{2} \cos \frac{k_x}{2}] \\
& + v_{r3}[\tau^y \mu^z \sigma^x \sin \frac{k_x}{2} \sin \frac{k_y}{2} + \tau^y \mu^x \sigma^y \sin \frac{k_y}{2} \sin \frac{k_z}{2} + \mu^y \sigma^z \sin \frac{k_z}{2} \sin \frac{k_x}{2}] \\
& + v_{s1}[\tau^x \sigma^x \sin \frac{k_x}{2} \cos \frac{k_y}{2} + \tau^x \mu^x \sigma^y \sin \frac{k_y}{2} \cos \frac{k_z}{2} + \mu^x \sigma^z \sin \frac{k_z}{2} \cos \frac{k_x}{2}] \\
& + v_{s2}[\tau^x \sigma^y \cos \frac{k_x}{2} \sin \frac{k_y}{2} + \tau^x \mu^x \sigma^z \cos \frac{k_y}{2} \sin \frac{k_z}{2} + \mu^x \sigma^x \cos \frac{k_z}{2} \sin \frac{k_x}{2}] \\
& + v_{s3}[\tau^x \mu^z \sigma^z \cos \frac{k_x}{2} \sin \frac{k_y}{2} - \tau^y \mu^y \sigma^x \cos \frac{k_y}{2} \sin \frac{k_z}{2} + \tau^z \mu^x \sigma^y \cos \frac{k_z}{2} \sin \frac{k_x}{2}] \\
& + v_2[\cos(k_x) + \cos(k_y) + \cos(k_z)].
\end{aligned} \tag{S-1}$$

The parameters in Figs. 2 and 3 are chosen following Ref. [34] as: $v_1 = 0.55, v_p = -0.76, v_{s1} = -0.04, v_{s2} = 0, v_{s3} = 0, v_{r1} = 0, v_{r2} = -0.03, v_{r3} = 0.01, v_2 = 0.16, \mu = 0.2$.

II. CONSTRUCTION OF WAVEFUNCTION AT Γ AND R POINT

In this section, we are going to construct the wavefunctions at two high symmetry points Γ and R , which are used to project the SC pairing onto the Fermi surfaces around the high symmetry points in the main text. At Γ and R , the non-symmorphic symmetry can be treated as its point group component which is independent with momentum k . Accordingly, we can use two $\mathbf{k} \cdot \mathbf{p}$ models near Γ and R instead of the continuum model. However, the $k \cdot p$ form is usually difficult to diagonalize. According to Ref. 33, the low energy Hamiltonian describing fourfold or sixfold degeneracies has a form $\mathbf{k} \cdot \mathbf{S}$, where \mathbf{S} is the vector of spin-3/2 or -1 matrices. Here, we will first project the $\mathbf{k} \cdot \mathbf{p}$ model into a $\mathbf{k} \cdot \mathbf{p}$ form and then project the corresponding eigenvectors onto the original $\mathbf{k} \cdot \mathbf{p}$ form.

After choosing linear terms originating from the tight-binding Hamiltonian expanded around Γ point ($H_\Gamma = H|_{k_x=k_y=k_z=0} + \delta k_x \frac{\partial H}{\partial k_x}|_{k_x=1, k_y=k_z=0} + \delta k_y \frac{\partial H}{\partial k_y}|_{k_x=0, k_y=1, k_z=0} + \delta k_z \frac{\partial H}{\partial k_z}|_{k_x=0, k_y=0, k_z=1}$), we obtain a $\mathbf{k} \cdot \mathbf{p}$ Hamiltonian near Γ as

$$\begin{aligned}
H_\Gamma = & v_1(\tau_x + \tau_x \mu_x + \mu_x) \\
& + v_p(\mu_y k_x + \tau_y \mu_z k_y + \tau_y \mu_x k_z) \\
& + v_{r1}(\tau_y \mu_z \sigma_y + \tau_x \mu_x \sigma_z + \mu_y \sigma_x) \\
& + v_{r2}(\tau_y \sigma_z + \tau_x \mu_y \sigma_x + \tau_z \mu_y \sigma_y) \\
& + v_{s1}(\tau_x \sigma_x k_x + \tau_x \mu_x \sigma_y k_y + \mu_x \sigma_z k_z) \\
& + v_{s2}(\tau_x \sigma_x k_x + \tau_x \sigma_y k_y + \tau_x \mu_x \sigma_x k_z) \\
& + v_{s3}(\tau_z \mu_x \sigma_y k_x + \tau_x \mu_z \sigma_z k_y - \tau_y \mu_y \sigma_x k_z) \\
& + 3v_2 - \mu_\Gamma.
\end{aligned} \tag{S-2}$$

which is constraint by the Little group isomorphic to point group \mathbb{T} .

Before deriving the eigenvector of Eq. (S-2), we construct the projection operator connect the $\mathbf{k} \cdot \mathbf{p}$ form to the $\mathbf{k} \cdot \mathbf{S}$ form with \mathbf{S} being the vector of spin-3/2 matrices. The spin-3/2 matrices can be view as a total angular momentum as a mixture of the p -orbital momentum $l=1$ and the electron spin momentum 1/2. The p -orbital momentum can be constructed from the matrix representations of the three generators at Γ . In particular, the representation G_1 and G_2 of the spinless screws operator \tilde{s}_{2x} and \tilde{s}_{2z} are commute with the representation G_3 of spinless threefold rotation $\tilde{C}_{3,111}$. The commutation relations read $G_1^2 = G_2^2 = G_3^3 = 1$, $[G_1, G_2] = 0$, $G_1 G_3 = G_3 G_2$, $G_2 G_3 = G_3 G_1 G_2$.

We find that these commutation relations are satisfied by the following spinless matrices

$$G_1 = \tau^x, \quad G_2 = \mu^x \quad \text{and} \quad G_3 = \begin{pmatrix} 1 & 0 & 0 & 0 \\ 0 & 0 & 1 & 0 \\ 0 & 0 & 0 & 1 \\ 0 & 1 & 0 & 0 \end{pmatrix}. \quad (\text{S-3})$$

Here, the eigenvalues of $G_1(G_2)$ are $m_x(m_z) = \pm 1$ and the corresponding eigenvectors are analogous to three p orbitals and one s orbitals. The s orbital with $(m_x, m_z) = (-1, 1)$ corresponds to a trivial representation and the three p orbitals under $SU(2)$ invariance form a 3d irreducible representation: p_x orbital with $(1, -1)$, p_y orbital with $(-1, -1)$, p_z orbital with $(-1, 1)$, which can be

$$\begin{aligned} p_x &= \frac{1}{2}(-1, 1, 1, -1) \\ p_y &= \frac{1}{2}(-1, 1, -1, 1) \\ p_z &= -\frac{1}{2}(-1, -1, 1, 1) \end{aligned} \quad (\text{S-4})$$

We express the three p orbitals as linear combinations with distinct angular momentum eigenvalues (l, m_l) : p_z orbital with $l = 0, m_l = 0$; $p_{\pm} = \frac{1}{\sqrt{2}}(p_x \pm ip_y)$ orbitals with $l = 1, m_l = \pm 1$. When coupled to the spin, the component of the total angular momentum along z direction $m_j = \pm \frac{3}{2}, \pm \frac{1}{2}$ is good quantum number to characterize the fourfold degenerate state at Γ . And the Clebsch-Gordan coefficients are assigned as $p_{\frac{3}{2}} = \tilde{p}_+ \otimes |\uparrow\rangle, p_{\frac{1}{2}} = \sqrt{\frac{1}{3}}\tilde{p}_+ \otimes |\downarrow\rangle + \sqrt{\frac{2}{3}}\tilde{p}_z \otimes |\uparrow\rangle, p_{-\frac{1}{2}} = \sqrt{\frac{1}{3}}\tilde{p}_- \otimes |\uparrow\rangle + \sqrt{\frac{2}{3}}\tilde{p}_z \otimes |\downarrow\rangle, p_{-\frac{3}{2}} = \tilde{p}_- \otimes |\downarrow\rangle$.

Thus we obtain the spin-3/2 matrices

$$\begin{aligned} p_{\frac{3}{2}} &= \frac{1}{\sqrt{2}} \left\{ \frac{1}{2} + \frac{i}{2}, 0, -\frac{1}{2} + \frac{i}{2}, 0, \frac{1}{2} - \frac{i}{2}, 0, -\frac{1}{2} + \frac{i}{2}, 0 \right\} \\ p_{\frac{1}{2}} &= \frac{1}{\sqrt{6}} \left\{ -1, \frac{1}{2} + \frac{i}{2}, -1, -\frac{1}{2} + \frac{i}{2}, 1, \frac{1}{2} - \frac{i}{2}, 1, -\frac{1}{2} + \frac{i}{2} \right\} \\ p_{-\frac{1}{2}} &= \frac{1}{\sqrt{6}} \left\{ -\frac{1}{2} + \frac{i}{2}, -1, \frac{1}{2} - \frac{i}{2}, -1, -(\frac{1}{2} + \frac{i}{2}), 1, \frac{1}{2} + \frac{i}{2}, 1 \right\} \\ p_{-\frac{3}{2}} &= \frac{1}{\sqrt{2}} \left\{ 0, -(\frac{1}{2} - \frac{i}{2}), 0, \frac{1}{2} - \frac{i}{2}, 0, -(\frac{1}{2} + \frac{i}{2}), 0, \frac{1}{2} + \frac{i}{2} \right\}. \end{aligned} \quad (\text{S-5})$$

It is worthwhile to note that they are related to each other by s_{2x} or \mathcal{T} .

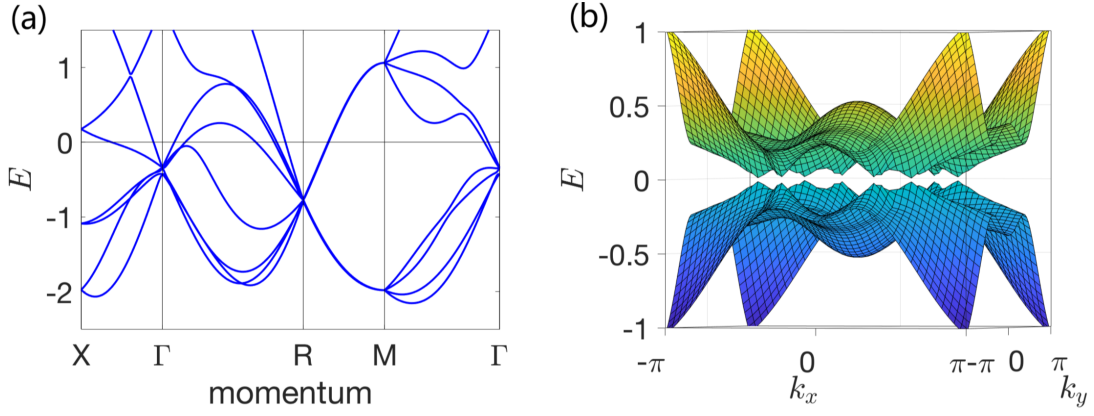
Now we can project the eight-band $\mathbf{k} \cdot \mathbf{p}$ Hamiltonian onto this basis $(p_{\frac{3}{2}}, p_{\frac{1}{2}}, p_{-\frac{1}{2}}, p_{-\frac{3}{2}})$. It becomes a four-dimensional $\mathbf{k} \cdot \mathbf{S}$ form. This can be understood since the Hamiltonian around Γ point is constraint by the Little group isomorphic to point group \mathbb{T} . The Hamiltonian at Γ point ($\vec{k} = 0$) has four-fold degenerate bands with the same mass m and it can be written into a four-dimensional linearized form around Γ .

$$H_{3/2} = m\mathbb{1} + a\delta\vec{k} \cdot \vec{S} + b\delta\vec{k}' \cdot \vec{S}' + c[S_z, (S_x S_x - S_y S_y)] \quad (\text{S-6})$$

where a, b and c are three independent real-valued parameters and $\mathbb{1}$ is a four-dimensional matrices. $\vec{S} = (S_x, S_y, S_z)$ and $\vec{S}' = (S_x^3, S_y^3, S_z^3)$, in which S_x, S_y , and S_z are spin-3/2 matrices:

$$S_x = \frac{1}{2} \begin{pmatrix} 0 & \sqrt{3} & 0 & 0 \\ \sqrt{3} & 0 & 2 & 0 \\ 0 & 2 & 0 & \sqrt{3} \\ 0 & 0 & \sqrt{3} & 0 \end{pmatrix}, \quad S_y = \frac{1}{2i} \begin{pmatrix} 0 & \sqrt{3} & 0 & 0 \\ -\sqrt{3} & 0 & 2 & 0 \\ 0 & -2 & 0 & \sqrt{3} \\ 0 & 0 & -\sqrt{3} & 0 \end{pmatrix}, \quad S_z = \frac{1}{2} \begin{pmatrix} 3 & 0 & 0 & 0 \\ 0 & 1 & 0 & 0 \\ 0 & 0 & -1 & 0 \\ 0 & 0 & 0 & -3 \end{pmatrix}. \quad (\text{S-7})$$

The two forms (Eqs. (S-2) and (S-6)) are related with $m = -m_{\Gamma} + 3v_q + v_{r1} - v_{r2} - \mu_{\Gamma}$, $a = \frac{1}{12}(14v_{s1} - 9v_{s2} + 9v_{s3} + 4v_{\Gamma})$, $b = \frac{1}{3}(-2v_{s1} + v_{s2} - v_{s3})$ and $c = \frac{1}{6}(v_{s2} + v_{s3})$.



Supplementary Figure S1. (Color online) (a) The bulk band structure for RhSi along high symmetry lines and (b) the surface states in the BdG spectrum with SC order parameter $\Delta = 0.5$. $v_{s1} = v_{s2} = -v_{s3} = -0.76$ and the other parameters are the same with Fig. 2(b).

It is easy to find the eigenstates at $b = c = 0$ and $m = 0$, by setting $v_{s1} = v_{s2} = -v_{s3}$ and $\mu_\Gamma = -m_\Gamma + 3v_q + v_{r1} - v_{r2}$. Note that although the parameters are changed to $v_{s1} = v_{s2} = -v_{s3} = -v_p$, the energy degeneracy at Γ and R are kept, as shown in Fig.S1(a). And the existence of TSC for the new set of parameters is established by Fig. S1(b).

The two eigenvectors of of Equation (S-6) with positive eigenvalues $\frac{3}{2}$ and $\frac{1}{2}$ are

$$\begin{aligned} \phi_{\Gamma,3/2} &= \frac{e^{-3i\phi}}{2\sqrt{2}} \left\{ - \left(\cos \frac{\theta}{2} - \sin \frac{\theta}{2} \right)^3, -\sqrt{3}e^{i\phi}(\sin \theta - 1) \left(\sin \frac{\theta}{2} + \cos \frac{\theta}{2} \right), \right. \\ &\quad \left. \sqrt{3}e^{2i\phi} \frac{(\sin \theta - 1)}{\cos \theta} \left(\sin \frac{\theta}{2} + \cos \frac{\theta}{2} \right)^3, e^{3i\phi} \left(\sin \frac{\theta}{2} + \cos \frac{\theta}{2} \right)^3 \right\} \\ \phi_{\Gamma,1/2} &= \frac{e^{-3i\phi}}{4} \left\{ -\sqrt{3}(\sin \theta - 1) \left(\sin \frac{\theta}{2} + \cos \frac{\theta}{2} \right), -e^{i\phi}(3 \sin \theta + 1) \left(\cos \frac{\theta}{2} - \sin \frac{\theta}{2} \right), \right. \\ &\quad \left. e^{2i\phi}(3 \sin \theta - 1) \left(\sin \frac{\theta}{2} + \cos \frac{\theta}{2} \right), e^{3i\phi} \frac{\sqrt{3} \cos^2 \theta}{\cos \frac{\theta}{2} - \sin \frac{\theta}{2}} \right\}. \end{aligned}$$

Accordingly, with $v_{s1} = v_{s2} = -v_{s3}$ and $\mu_\Gamma = -m_\Gamma + 3v_q + v_{r1} - v_{r2}$, the eigenstate of Eq. (S-2) can be easily obtained $|\psi_{\Gamma,i}\rangle = |\phi_{\Gamma,i}\rangle \langle p_{\frac{3}{2}}, p_{\frac{1}{2}}, p_{-\frac{1}{2}}, p_{-\frac{3}{2}} |$.

$(|\psi_{\Gamma,3/2}\rangle$ and $|\psi_{\Gamma,1/2}\rangle)$ are the time-reversal partners of each other after fixing the phase.

Similarly, we can expand the Hamiltonian near R point ($H|_{k_x=k_y=k_z=\pi} - \delta k_x \frac{\partial H}{\partial k_x}|_{k_x=\pi, k_y=k_z=0} - \delta k_y \frac{\partial H}{\partial k_y}|_{k_x=0, k_y=\pi, k_z=0} - \delta k_z \frac{\partial H}{\partial k_z}|_{k_x=0, k_y=0, k_z=\pi}$ and obtain

$$\begin{aligned} H_R &= +v_p(\tau_y \mu_z k_x + \tau_y \mu_x k_y + \mu_y k_z) \\ &\quad + v_{r3}(\tau_y \mu_z \sigma_x + \tau_y \mu_x \sigma_y + \mu_y \sigma_z) \\ &\quad + v_{s1}(\mu_x \sigma_z k_x + \tau_x \mu_x \sigma_x k_y + \tau_y \mu_x \sigma_y k_z) \\ &\quad + v_{s2}(\tau_x \sigma_y k_x + \tau_x \mu_x \sigma_z k_y + \mu_x \sigma_x k_z) \\ &\quad + v_{s3}(\tau_x \mu_z \sigma_z k_x - \tau_y \mu_y \sigma_x k_y + \tau_z \mu_x \sigma_y k_z) \\ &\quad - 3v_2 - \mu_R. \end{aligned} \tag{S-8}$$

At R , the Hamiltonian is six-fold degenerate and a three-dimensional irreducible representation can be given by the three generators

$$s_{2x}^R = \{C_{2x}|\frac{1}{2}\frac{3}{2}0\}, s_{2y}^R = \{C_{2y}|0\frac{1}{2}\frac{3}{2}\}, \text{ and } s_3 = \{C_{3,111}^{-1}|010\}. \tag{S-9}$$

They satisfy $\{C_{3,111}^{-1}|010\}^3 = \{\mathcal{R}|111\}$, $\{C_{2x}|\frac{1}{2}\frac{3}{2}0\}^2 = \{\mathcal{R}|100\}$, $\{C_{2z}|0\frac{3}{2}\frac{1}{2}\}^2 = \{\mathcal{R}|030\}$, and thus are different from the generators at Γ .

Similar to the matrices at Γ without SOC, the representation at R is $[s_{2xR}, s_{2zR}] = 0$ and can be form a 3d irreducible representation. We take one of the p 's in the 3d irreducible basis p_R and its C_3 rotation partner $|p_R\rangle, G_3|p_R\rangle$ and $G_3^2|p_R\rangle$ form a 3d representation, while their time-reversal partners ($\mathcal{T}|p_R\rangle, G_3\mathcal{T}|p_R\rangle$ and $G_3^2\mathcal{T}|p_R\rangle$) consist another 3d representation. In combination, a six-dimensional (6d) basis is formed

$$\{|p_R\rangle, G_3|p_R\rangle, G_3^2|p_R\rangle, \mathcal{T}|p_R\rangle, G_3\mathcal{T}|p_R\rangle, G_3^2\mathcal{T}|p_R\rangle\}. \quad (\text{S-10})$$

which gives a 6d representation of the Hamiltonian in a $\delta\mathbf{k} \cdot \mathbf{S}$ form.

To construct this 6D representation for SG P2₁3 at R , we note that the unitary subgroup of the little group is isomorphic to the little group of SG 199 and satisfies

$$H_{198}(\delta\mathbf{k}) = \begin{pmatrix} H_{199}(a, \delta\mathbf{k}) & bH_{199}(1, \delta\mathbf{k}) \\ b^*H_{199}(1, \delta\mathbf{k}) & -H_{199}^*(a, \delta\mathbf{k}) \end{pmatrix} \quad (\text{S-11})$$

where the Hamiltonian for SG 199 is given by Gell-Mann matrices as

$$H_{199} = \begin{pmatrix} 0 & a\delta k_x & a^*\delta k_y \\ a^*\delta k_x & 0 & ak_z \\ ak_y & a^*k_z & 0 \end{pmatrix} \quad (\text{S-12})$$

with $a = |a|e^{i\eta}$ is a complex parameters.

When $\eta = \frac{\pi}{6}$, we note that Eq.(S-11) can be exactly solvable. The eigenvector above the fermi surfaces is

$$\phi_{R,-1} = \left\{ 0, 0, 0, \frac{(1-i)(3+\sqrt{3})\cos\theta}{(3+(2+i)\sqrt{3})(\sin\theta\cos(\phi)+i\sin(\phi))}, \frac{(\sqrt{3}-i)(\cos(\phi)+i\sin\theta\sin(\phi))}{2\sin\theta\cos(\phi)+2i\sin(\phi)}, 1 \right\}$$

When the eigenvectors projected onto p orbitals basis, they are written into eight-dimensional vectors $|\psi_{R,-1}\rangle = |\phi_{R,-1}\rangle\langle p_1, p_0, p_{-1}|$. While $|\psi_{R,1}\rangle$ can be utilized to project the Hamiltonian to one of the Fermi surfaces with $\mathcal{C} = -2$ around R , its time-reversal partner $\mathcal{T}|\psi_{R,1}\rangle$ project to the other Fermi surface.